Journal of Materials Chemistry A

PAPER

View Article Online
View Journal | View Issue

Bulk crystal seeding in the generation of mesopores by organosilane surfactants in zeolite synthesis†

Cite this: J. Mater. Chem. A, 2014, 2, 11905

Jaeheon Kim,[ab] Changbum Jo,*[a] Seungjun Lee[ab] and Ryong Ryoo*[ab]

Received 19th April 2014
Accepted 15th May 2014

DOI: 10.1039/c4ta01948b

www.rsc.org/MaterialsA

Zeolites of MOR, CHA, and FAU-X topologies were conventionally synthesized using Na^+ or an organic structure-directing agent, except that organosilane surfactants were added as a mesopore-generating agent. The organosilanes were represented by the structural formula $(CH_3O)_3Si–C_3H_6–N^+(CH_3)_2C_nH_{2n+1}$, where n was varied from 12 to 16 and 18. Each zeolite synthesis was seeded with a small amount of bulk zeolites of the same structure type. The synthesis result indicated that the bulk zeolite seeds disappeared completely from the zeolite products, indicating their disintegration into tiny fragments that were undetectable by high-resolution transmission electron microscopy. Nevertheless, the zeolite seeding caused a dramatic decrease in synthesis time. More importantly, crystal seeding, in comparison to unseeded synthesis, was highly effective in extending the organosilane-directed mesopore-generating strategy to a wide range of mesoporous and zeolite structures.

1. Introduction

Zeolites containing secondary mesopores in addition to the framework structural micropores are referred to as 'hierarchically nanoporous zeolites' or 'hierarchical zeolites'.[1,2] Hierarchical zeolites usually have morphologies of nanorods, nanosheets, and nanosponges, and typically have a thickness range of 2–50 nm at the mesoscale. Such zeolite nanocrystals are built with crystalline microporous frameworks.[3] The nanocrystals are loosely interconnected so that the intercrystalline void space becomes mesoporous. These mesopores become a highway for the rapid diffusion of adsorbate species to the nanocrystals.[4–7] Compared to conventional bulk zeolites composed of much larger crystals (*e.g.*, several micrometres in diameter), rapid molecular diffusion to hierarchical zeolites often leads to significantly improved catalytic activity and lifetime in various reactions.[7]

In addition to their superior molecular diffusion properties, hierarchical zeolites possess strong Brønsted acid sites on mesopore walls (*i.e.*, external surfaces).[8] The external acid sites are accessible to bulky molecules that are too large to enter ordinary zeolite micropores.[4,9] The acid strength is high in comparison to the internal acid sites (*i.e.*, acid sites located on the framework constituting internal micropores). With these features, hierarchical zeolites are suitable as solid acid catalysts for reactions involving bulky molecules.[10] Mesopores in hierarchical zeolites are also suitable as hosts for catalytic materials.[11–14] Lee *et al.* demonstrated that organic functional groups could be covalently grafted onto mesopore walls in an MFI zeolite nanosponge that was synthesized using an organosilane surfactant as the mesopore-generating agent.[13] The organic groups could effectively chelate transition metal complexes for the catalytic application in C–C coupling reactions. Recently, Jo *et al.* synthesized another type of MFI zeolite nanosponge that exhibited a narrow distribution of pore diameters centered at 4 nm.[15] Kim *et al.* supported 10 wt% cobalt onto this zeolite nanosponge through the impregnation of cobalt nitrate.[14] They reported that Co/MFI zeolites prepared in this manner contained uniform-sized cobalt nanoparticles with about the same diameters as the mesopores in the zeolites. This Co/MFI catalyst exhibited a remarkably high conversion of CO and high selectivity for branched hydrocarbons in the gasoline range in Fischer–Tropsch synthesis. As these examples show, uniform mesopores in hierarchical zeolites provide an ideal space for supporting metal and metal oxide nanoparticles.[14]

Due to the importance of a new class of mesoporous catalytic materials equipped with strong acid sites, a number of direct synthesis or post-synthetic methods have been proposed for hierarchical zeolites in recent years.[16–20] For example, pre-synthesized bulk zeolites were treated with an aqueous solution of an acid or base to generate mesopores through local dissolution.[17,18] In other studies, nanostructured carbons or polymer nanoparticles were incorporated into a zeolite synthesis gel composition as a template for mesopores.[19,20] Organosilane surfactants have also been added to a zeolite synthesis composition as a mesopore-generating agent.[16] Moreover,

[a]Center for Nanomaterials and Chemical Reactions, Institute for Basic Science (IBS), Daejeon 305-701, Republic of Korea. E-mail: jochangbum@kaist.ac.kr; rryoo@kaist.ac.kr; Fax: +82-42-350-8130; Tel: +82-42-350-2870

[b]Department of Chemistry, KAIST, Daejeon 305-701, Republic of Korea

† Electronic supplementary information (ESI) available: Additional SEM and TEM images of *s*-MOR, *s*-CHA, and *s*-FAU-X, the N_2 isotherm and pore size distribution of *s*-MOR, XRD patterns for bulk CHA, *s*-CHA, and *us*-CHA. See DOI: 10.1039/c4ta01948b

multiammonium surfactants have been used as a mesopore–micropore dual structure-directing agent (SDA).[21] Each of these methods has its own advantages and disadvantages, depending on synthesis quantities and application purposes. The present study focuses on the use of organosilane, as this method has the advantage of being applicable for various zeolites using the same organosilane. The organosilane surfactants have a $[(MeO)_3Si-]$ moiety connecting an alkylammonium head group and a long alkyl tail. The MeO–Si bonds can readily be hydrolyzed to HO–Si under zeolite synthesis conditions. Therefore, the silane moiety can form Si–O–Si or Si–O–Al covalent bonds with other silica and alumina sources. At the same time, the alkyl tails become associated into a micelle due to hydrophobic interactions. This leads to the generation of mesopores with uniform diameters within zeolites. Choi *et al.* used the organosilane method for the synthesis of hierarchical MFI and zeolite A [designated by 'LTA' according to the 3-letter framework type code of the International Zeolite Association (IZA)].[16] The mesopore diameters of these zeolites could be systematically tailored to be in the range of 2–4 nm by changing the length of the alkyl tails. This method could be extended to chabazite and faujasite-X (designated by 'CHA' and 'FAU-X', respectively, according to the 3-letter framework type code of IZA) as well as zeolite analogues with $AlPO_4$-5 and $AlPO_4$-11 (designated by 'AFI' and 'AEL', respectively, according to the 3-letter framework type code of IZA).[22–24] In the MFI and LTA zeolites, the mesopore volumes could be continuously increased by increasing the loading of organosilane to 5 mol% of the total silica source. However, this method had limited success in other zeolites. The mesopore generation was reported to be effective only below 2 mol% organosilane in CHA, FAU-X, AFI, and AEL zeolites.[22–24] Zeolites synthesized with more than 2 mol% have been reported to contain impurity phases, such as zeolite P (designated by 'GIS' according to the 3-letter framework type code of IZA) and amorphous aluminosilicates. The organosilane approach was also examined for the synthesis of mordenite (designated by 'MOR' according to the 3-letter framework type code of IZA) in an early stage of the present investigation. However, the simple addition of organosilane surfactants in the MOR zeolite synthesis was not effective at all. Thus, the organosilane-directed method has only had limited success so far.

The present work was undertaken to resolve the limitation for mesopore generation of organosilane surfactants in the synthesis of hierarchical zeolites and thereby extend the applicability of the organosilane method. To this end, we tested various surfactants with modification of the organosilane moiety between the ammonium head group and the alkyl tail. We also tested organosilane surfactants with multiammonium groups. However, the structure modification of organosilane was not satisfactory for this purpose. After all, a much more effective method was the simple addition of a small amount of bulk zeolites as seeds to a zeolite synthesis composition containing the organosilane surfactant, before hydrothermal reaction. The addition of zeolite seeds into the zeolite synthesis composition is a well-known method for decreasing the required hydrothermal synthesis time and widening the available synthesis region for zeolites.[15,25–27] In this paper, we report the zeolite-seeding effect for the synthesis of hierarchical MOR, CHA, and FAU-X zeolites.

2. Experimental

2.1 Reagents

Fumed silica, sodium silicate solution (26.5 wt% SiO_2, 10.6 wt% Na_2O), sodium aluminate (53.0 wt% Al_2O_3, 42.5 wt% Na_2O), and aluminium hydroxide $[Al(OH)_3 \cdot xH_2O]$ were purchased from Aldrich and used as received. Sodium hydroxide (NaOH, 98%, Junsei), tetraethylammonium bromide (TEABr, 98%, TCI), benzene (99.5%, Junsei), and benzyl alcohol (98%, Aldrich) were also used as received. *N*,*N*,*N*-trimethyl-1-adamantaneammonium hydroxide (TMAdOH) was synthesized by alkylation of 1-adamantane amine (98%, Aldrich) with methyl iodide (97%, Junsei) in the presence of sodium bicarbonate (99%, Junsei) and the subsequent anion exchange of I^- to OH^-, following a published procedure.[20] A series of organosilane surfactants was obtained following the synthesis procedure in the literature.[7] These organosilanes are represented by the structural formula $(CH_3O)_3Si–C_3H_6–N^+(CH_3)_2–C_nH_{2n+1}$, where n is varied from 12 to 16 and 18. For brevity, the organosilanes are denoted as 'OS-n'.

2.2 Synthesis of zeolites

2.2.1 Seed zeolites. Three types of bulk zeolites (MOR, CHA, and FAU-X) were hydrothermally synthesized following procedures reported in the literature.[28–30] The zeolite samples with bulk crystalline morphologies were calcined at 550 °C for 5 h, before being used as seeds in the organosilane-directed synthesis.

2.2.2 Hierarchical MOR. We dispersed 0.04 g of bulk MOR zeolites into 4.0 ml of 0.25 M aqueous solution of NaOH in a polypropylene bottle. After stirring at 60 °C overnight, 0.78 g of fumed silica was added at once to the reaction mixture, and immediately shaken by hand for 15 min. We added 2.5 ml of distilled water containing 0.18 g of sodium aluminate to this solution. The resultant mixture was vigorously shaken by hand for 15 min, and subsequently we added 0.53 M aqueous solution of TEABr. The resultant gel (Mixture A) was aged for 1 h at room temperature. Meanwhile, 0.72 g of OS-12 (60 wt% solution in methanol) and 10 ml of 1 M aqueous solution of NaOH were mixed in another propylene bottle until a clear solution was obtained (Mixture B). Then, we poured 'Mixture B' into 'Mixture A' at once under vigorous magnetic stirring. The entire mixture was stirred for 6 h at room temperature to make a homogeneous gel. The mixture had the molar composition of 100 SiO_2/7 Al_2O_3/21 Na_2O/4.2 TEABr/3750 H_2O/4.5 OS-12. This gel mixture was transferred to a Teflon-lined stainless-steel autoclave and heated with tumbling at 140 °C for 4 days. The product was filtered, washed with distilled water, and dried at 100 °C. The resultant sample was calcined at 550 °C for 4 h in air. For catalytic tests, the calcined zeolite sample was ion-exchanged with NH_4^+ using 1 M aqueous solution of NH_4NO_3 at room temperature. Then, the ion-exchanged sample was calcined at 550 °C to convert to the H^+-form.

2.2.3 Hierarchical CHA. We dispersed 0.03 g of bulk CHA zeolites into 4.0 ml of 0.25 M aqueous solution of NaOH in a polypropylene bottle, and stirred at 60 °C overnight. Then, 0.57 g of fumed silica was added at once to this solution, and immediately shaken by hands for 15 min. We added 0.9 ml of 2.5 M aqueous solution of TMAdOH containing 0.05 g of aluminium hydroxide to this mixture. The resultant mixture (Mixture C) was aged for 1 h at room temperature. Meanwhile, 0.41 g of OS-18 was dissolved in 0.9 ml of 2.5 M aqueous solution of TMAdOH in another propylene bottle (Mixture D). Then, 'Mixture D' was added to 'Mixture C' at once. The entire mixture had the molar composition of 100 SiO_2/2.5 Al_2O_3/10 Na_2O/20 TMAdOH/4000 H_2O/4 OS-18. This gel composition is the same as that previously reported by Wu *et al.*[22] The remainder of the synthesis was the same as that for the MOR zeolites described in Section 2.2.2, except for a change in hydrothermal reaction time to 2.5 days.

2.2.4 Hierarchical FAU-X. We mixed 2.20 g of sodium silicate solution with 3.15 ml of 0.1 M aqueous solution of NaOH in a polypropylene bottle. Then, 0.03 g of bulk FAU-X zeolites was added to this solution. After stirring at 60 °C overnight, 0.25 g of OS-18 dissolved in 0.1 M aqueous solution of NaOH (3.1 ml) was added under vigorous magnetic stirring. After further aging for 1 h at room temperature, the resultant gel was mixed with 3.1 ml of distilled water containing 0.63 g of sodium aluminate, and subsequently stirred for 12 h at room temperature. The final gel had the molar composition of 100 SiO_2/33 Al_2O_3/117 Na_2O/6000 H_2O/3 OS-18. The remainder of the synthesis was the same as that for the MOR zeolites described in Section 2.2.2, except for changes in the hydrothermal temperature to 60 °C and the reaction time to 2.5 days.

2.3 Carbon replications of MOR zeolites

0.25 g of sucrose (Junsei) was dissolved in 0.38 g of distilled water containing 0.015 ml of sulfuric acid (95%, Junsei). Then, MOR zeolites were infiltrated with the mixture consisting of sucrose and sulfuric acid. The added amount of MOR zeolites was adjusted to have the ratio of (total pore volume of the zeolite sample)/(1 g of sucrose) to be 1.25. The infiltrated MOR zeolites were dried at 100 °C for 6 h. Subsequently, the temperature was increased to 160 °C and retained for 6 h. The carbon/zeolite composite after heating was infiltrated again with 65% of the amount of the mixture, which was first infiltrated. After heating to 160 °C for 6 h again, the black powder was placed in a quartz tube, heated to 450 °C for 3 h, and maintained for 1 h at the same temperature. Then, the temperature was further increased to 700 °C for 2 h, and retained for 4 h. The MOR zeolites in the composite products were selectively removed by washing with an excessive amount of HF and HCl mixture solution.

2.4 Friedel–Crafts alkylation of benzene with benzyl alcohol

We degassed 50 mg of the H^+-form of the zeolite sample at 300 °C using a PYREX® reactor. After cooling to room temperature, the PYREX® reactor was transferred into a glove box that was filled with N_2. Then, a mixture of benzene (17.5 ml) and benzyl alcohol (0.9 ml) was fed into the PYREX® reactor. This reactor was heated for 80 h under stirring at 80 °C to conduct the catalytic reaction. During the reaction, small aliquots of the liquid sample were taken at regular time intervals. The samples were analysed by a gas chromatograph (GC, Younglin, Acme-6000) after separation of the zeolite catalyst by filtration. The gas chromatograph was equipped with a flame ionization detector and a HP-Innowax capillary column (J & W scientific: 30 m long, 0.32 mm i.d., and 0.25 μm thickness).

2.5 Characterization

X-ray diffraction (XRD) patterns were taken from powder samples using a Rigaku Multiflex diffractometer with a nickel-filtered Cu Kα radiation beam (40 kV, 30 mA). Scanning electron microscopy (SEM) images were taken with an FEI Verios230 instrument operating at 1.0 kV using beam deceleration mode. Cross-section SEM images were taken with a Hitachi S-4800 instrument operating at 2.0 kV without a metal coating, after the zeolite crystallites were polished for 6 h using accelerated argon ions (6 kV, 120 μA) with a JEOL SM-09010. Transmission electron microscopy (TEM) images were taken with Tecnai G2 F30 using an operating voltage of 300 kV. N_2 adsorption–desorption isotherms were measured with a Micromeritics TriStar 2 volumetric adsorption analyser at the liquid nitrogen temperature. Prior to the adsorption analysis, all samples were degassed under vacuum for 5 h at 300 °C. The Brunauer–Emmett–Teller (BET) equation was used to calculate the specific surface area from the adsorption branch in the range of $P/P_0 =$ 0.05–0.20. The total pore volume was derived using the amount of N_2 adsorbed at $P/P_0 = 0.95$. The contents of Si and Al in the zeolite samples were determined by inductively coupled plasma-atomic emission spectroscopy (ICP-AES) using an OPTIMA 4300 DV instrument (Perkin Elmer).

3. Results and discussion

3.1 Synthesis of hierarchical MOR zeolites

Fig. 1a shows XRD patterns of the three MOR zeolite samples synthesized in the present work. Of these samples, the sample denoted as '*c*-MOR' was a MOR zeolite synthesized following a conventional synthesis procedure (*i.e.*, without using organosilane) as described in the Experimental section. The other two samples ('*s*-MOR' and '*us*-MOR') were both synthesized using organosilane as a mesopore-generating agent; however, the two samples differed in their seeding (Table 1). Specifically, the *s*-MOR sample was synthesized by seeding with bulk MOR zeolites, and the *us*-MOR sample was not seeded. As shown in the XRD pattern for the *c*-MOR sample, the zeolite crystallization resulted in highly phase-pure MOR zeolites in 3 days at 170 °C. However, in the case of the organosilane method, the hydrothermal temperature had to be maintained at 140 °C. This was because the organosilane decomposed under the strongly basic synthesis condition at temperatures above 150 °C. The zeolite formation at 140 °C proceeded very slowly. The MOR zeolite synthesis using organosilane had to be performed for 14 days to complete the zeolite crystallization. However, during this prolonged hydrothermal reaction time, the resultant *us*-

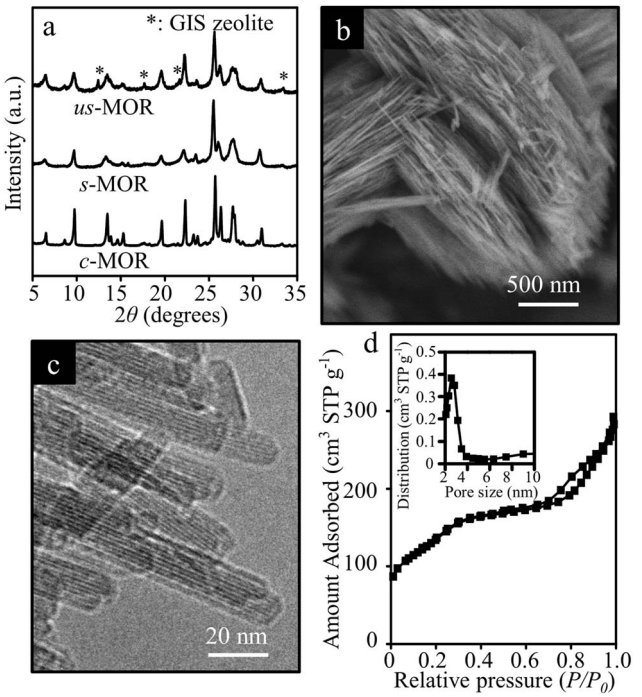

Fig. 1 (a) XRD pattern, (b) SEM image, (c) TEM image, and (d) N_2 adsorption-desorption isotherm of *s*-MOR. Pore size distribution of *s*-MOR derived from the adsorption isotherm using the BJH method was included as the inset of (d). In (a), the *s*-MOR zeolites were compared with the control sample synthesized without seeding (*us*-MOR), and the conventional MOR zeolites (*c*-MOR).

MOR product became heavily contaminated with GIS zeolites as an impurity phase (see the XRD pattern in Fig. 1a). To decrease the synthesis time, a bulk MOR zeolite (lab-made, amounting to 5 mol% of the total silica source) was added to the initial gel composition. In this case, a high-purity MOR zeolite was synthesized in only 4 days, indicating a dramatic decrease of the zeolite crystallization time. Moreover, this high-purity MOR zeolite collected in 4 days had nanorod morphologies. No amorphous phases could be detected by TEM or SEM (Fig. 1 and S1†), and the XRD pattern did not exhibit peak characteristics of GIS zeolites (see the XRD pattern in Fig. 1a). Compared to *c*-MOR, the *s*-MOR sample synthesized in this manner exhibited conspicuous line broadening in the *hk*0 reflections. This is in agreement with nanorod-like crystal morphologies with a narrow a–b cross section (see SEM and TEM images in Fig. 1b and c). Typical diameters of the zeolite nanorods ranged from 5 to 12 nm, as judged by TEM investigation (Fig. 1c and S1†). High-resolution TEM images and fast Fourier transform (FFT) images of the zeolite nanorods revealed that the *c*-axis of the MOR crystal structure was parallel to the longest edge of the nanorods (Fig. S2†). The bulk MOR particles, used for seeding, could not be found in the SEM and TEM images.

The porous texture of the *s*-MOR sample was analysed by N_2 adsorption measurements, in comparison with *c*-MOR. Fig. 1d shows the N_2 adsorption–desorption isotherms and their corresponding pore size distributions. The result from the MOR zeolite nanorods (*s*-MOR) shows a sharp increase in the relative pressure region, $0.2 < P/P_0 < 0.3$. This increase can be interpreted as the existence of mesopores that suddenly adsorb a large amount of N_2 due to capillary condensation in this pressure region. The mesopore size distribution of *s*-MOR can be derived from the adsorption branch of the N_2 isotherm using the Barrett–Joyner–Halenda (BJH) algorithm. The pore size distribution analysed in this manner exhibited a narrow peak centered at 2.6 nm (Fig. 1d). The mode value of mesopore diameters could be controlled over the range of 2.6 to 4.3 nm by changing the tail length of the organosilanes (Fig. S3†). Such a systematic control of mesopore diameters supported that the mesopores were generated by the micellar assembly of the organosilane surfactant. Due to the presence of the mesopores, *s*-MOR zeolites exhibited a large BET surface area (480 $m^2\ g^{-1}$) and total pore volume (0.41 $cm^3\ g^{-1}$). On the other hand, the bulk MOR zeolites (*c*-MOR) exhibited negligible mesopore capillary condensation in the N_2 adsorption isotherm. Our analysis of the adsorption isotherm showed a much less pore volume for *c*-MOR (total pore volume = 0.17 $cm^3\ g^{-1}$, BET surface area = 327 $m^2\ g^{-1}$) than for *s*-MOR.

It is particularly noteworthy that the bulk zeolite seeds were not detected at all by TEM and SEM, throughout all zeolite products. This result indicates that the micrometre-sized bulk additives must have disintegrated into tiny fragments, with sizes less than the a–b cross-section of the MOR nanorods. The marked decrease in the zeolite crystallization time by the crystal seeding, as mentioned above (4 days for *s*-MOR *vs.* 14 days for *us*-MOR), supports that the zeolite fragments acted as nuclei for MOR crystals to grow without a long induction period. The decrease in the crystallization time is important for generating phase-pure MOR zeolites with a high specific volume of mesopores. The organosilane compound used in the present synthesis often promotes the formation of GIS zeolites under highly basic synthesis conditions, such as those for LTA, FAU-X, and MOR. GIS zeolites can appear as impurities under a high concentration of the present organosilane in the zeolite synthesis.[24] This problem becomes more severe with increasing crystallization time. Rapid synthesis is important in the organosilane-directed synthesis, not only to prevent the formation of GIS zeolites, but also to achieve the high volume of mesopores. With increasing crystallization time, the Ostwald ripening type of zeolite recrystallization can occur under strong basic conditions, leading to a conversion of hierarchical zeolites to bulk zeolites.[16]

Another notable feature of the organosilane-directed MOR zeolite synthesis with bulk crystal seeding is that the diameter of the MOR nanorods can be precisely controlled according to the amount of the organosilane surfactant. To demonstrate this feature, the seeded MOR zeolites were synthesized with various amounts of OS-12 over the range of 1.5–4.5 mol% of the silica source. Mesoporous carbon was synthesized using each of the zeolite products as a template, as in the synthesis of CMK-1 mesoporous carbons.[31] The diameters of mesopores in the carbon replica were then analysed using N_2 adsorption. The mesopore diameters were assumed to be the same as the cross-sectional diameters of MOR nanorods in the synthesized products. The distribution of the nanorod diameters, obtained in this manner, is presented in Fig. 2a. As this result shows, the mode value of the

Table 1 Synthesis conditions and textural properties of *s*-MOR, *us*-MOR, *s*-CHA, *us*-CHA, *s*-FAU-X, and *us*-FAU-X

Sample	Reaction temperature (°C)	Reaction time (days)	Zeolite product	D_{meso}[a] (nm)	S_{BET}[b] ($m^2\ g^{-1}$)	V_{total}[c] ($cm^3\ g^{-1}$)
s-MOR	140	4	MOR nanorod	2.6	480	0.41
us-MOR	140	14	MOR nanorod + GIS	n.d.[d]	n.d.	n.d.
s-CHA	140	2.5	Mesoporous CHA	3.5	725	0.58
us-CHA	140	14	Mesoporous CHA + bulk CHA	20[e]	627	0.51
s-FAU-X	60	2.5	Mesoporous FAU-X	5	693	0.50
us-FAU-X	60	8	Mesoporous FAU-X + GIS	n.d.	n.d.	n.d.

[a] Mode value of the mesopore diameter derived from the adsorption branch of N_2 adsorption using the BJH method. [b] BET surface area. [c] Total pore volume derived from the amount of adsorbed N_2 at $P/P_0 = 0.95$. [d] Not determined. [e] Broad distributions of mesopores ranged from 15–25 nm.

zeolite nanorods was decreased from 17 to 9 nm as the OS-12 loading was increased from 1.5 to 4.5 mol%. The nanorod diameters, derived from carbon replication, were consistent with TEM measurements. Our successful range of seeded MOR synthesis was within 4.5 mol% of OS-12. The hydrothermal synthesis product, with OS-12 more than 4.5 mol%, contained amorphous aluminosilicate gel in addition to MOR zeolite nanorods. This is probably due to the decomposition of OS-12 by Hoffmann elimination before the full crystallization of zeolites, whereas zeolite crystallization is slower at a high loading of OS-12.

3.2 Widening of the mesopore-generating region

As mentioned in the previous section, the most important effect of crystal seeding in the MOR zeolite synthesis was the rapid generation of target zeolites before the formation of any impurity phases. In this section, we investigate if crystal seeding would also be effective in the organosilane-directed synthesis of other hierarchical zeolites, such as CHA and FAU-X frameworks. The synthesis of hierarchical CHA and FAU-X zeolites using organosilane surfactants was recently reported by other laboratories.[22,23] However, the mesopore generation in these zeolites by organosilane surfactants had only limited effectiveness at organosilane loadings less than 2 mol%. At higher loadings, the zeolite formation required long hydrothermal synthesis times. During the prolonged synthesis times, the product purity decreased due to the formation of impurities such as GIS, MFI and LTA zeolites. Therefore, we tested the crystal seeding effect for the synthesis of the CHA and FAU-X zeolites using OS-18 (Table 1). Our synthesis experiments were performed in exactly the same manner as described in previous studies,[22,23] except for the use of 5 mol% corresponding bulk zeolites for seeding. The seed crystals were added to the synthesis gel compositions prior to heating to the synthesis temperature, as in the synthesis of MOR zeolites. The reaction temperature was 140 °C for CHA zeolites, and 60 °C for FAU-X zeolites. Our synthesis results indicated that the required time for complete crystallization of the target zeolites was only 2.5 days, even when the organosilane loading was increased to 3–4 mol%. When the same zeolites were synthesized without seeding, the zeolite formation in the control synthesis experiments took more than three times longer. The unseeded zeolite products contained a large amount of bulk zeolites, such as CHA, FAU-X, and GIS zeolites. In contrast, the seeded products were high-quality mesoporous zeolites without impurities. Besides, the mesopore diameters were very uniform. The details of the results are described in the following paragraph. For brevity, the seeded zeolite samples are denoted as *s*-CHA and *s*-FAU-X and the unseeded samples are denoted as *us*-CHA and *us*-FAU-X.

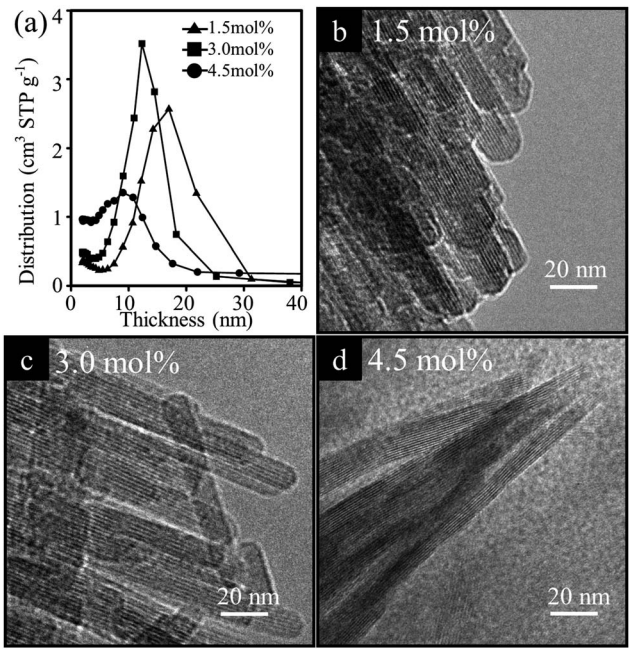

Fig. 2 (a) Pore size distributions of the carbon replicas of hierarchical MOR zeolites, which were synthesized using 1.5 mol%, 3.0 mol%, and 4.5 mol% of OS-12 in the presence of bulk MOR zeolite seeds. The pore size distributions of the carbon replicas represented the framework thickness distributions of the hierarchical MOR zeolites. (b, c and d) TEM images of hierarchical MOR zeolites, which were synthesized using 1.5 mol%, 3.0 mol%, and 4.5 mol% of OS-12.

The hydrothermal synthesis of *us*-CHA using 4 mol% OS-18 took at least 8 days before the products became fully crystalline zeolites without aluminosilicate residues. In contrast, the synthesis of *s*-CHA with the same OS loading was accomplished in 2.5 days. Both the *s*-CHA and *us*-CHA products exhibited XRD peaks that matched well with the CHA framework structure (Fig. S4†). Their Si/Al ratios were very similar (~12). However, as a result of seeding, there were remarkable changes in the particle morphologies and pore textural properties (Fig. 3). In

us-CHA, the central core of each particle was bulk CHA (see the cross-section SEM image in Fig. 3a, and SEM images in Fig. S5†), and only the outer portion was mesoporous CHA. The generation of such composite morphologies can be interpreted as follows: organosilanes could not be incorporated in an early stage of crystallization, and the CHA zeolites could be crystallized with bulk crystal morphology to form a central core. As fumed silica became depleted as a favourable silica source in the hydrothermal synthesis medium, the organosilane was able to participate in the zeolite formation. This seemed to cause the overgrowth of a mesoporous CHA shell on top of the CHA core crystal. The average porosity of *us*-CHA was characterized by N_2 adsorption–desorption isotherms. A pore size analysis derived from the N_2 adsorption isotherm indicated that the mesopores had a wide distribution of diameters ranging from 10 to 30 nm. These pore diameters were much larger than that which could be expected from a diameter of cylindrical or sheet-like micelles resulting from the OS-18 surfactant. Therefore, we believe that the OS-18 surfactant micelles self-expanded by the incorporation of other OS-18 molecules inside the core of the micelles. A similar phenomenon was reported in our previous synthesis work on hierarchical LTA zeolites using organosilanes. The mesopore diameter in the LTA zeolites increased progressively according to the OS loading.[32] In addition to this phenomenon, the mesoporous morphology was unstable under the prolonged synthesis time. The mesopores disappeared almost completely when *us*-CHA was filtered after hydrothermal synthesis for 14 days at 140 °C. This change can be explained by the Ostwald-ripening type of recrystallization processes.[16]

Unlike the core–shell separation of mesopores in *us*-CHA (synthesized for 8 days), the *s*-CHA sample (synthesized for 2.5 days) exhibited a uniform distribution of mesopores throughout the whole particle diameter in the cross-section SEM image shown in Fig. 3b (see Fig. S6† for SEM image). The TEM image in Fig. 3c agrees with a uniform distribution of mesopores in a particle (see Fig. S6† for a low magnification TEM image). Due to the presence of more highly dispersed mesopores, the *s*-CHA zeolites exhibited a larger BET surface area (725 $m^2\ g^{-1}$) and total pore volume (0.58 $cm^3\ g^{-1}$) than those of bulk CHA zeolites (BET surface area = 601 $m^2\ g^{-1}$, total pore volume = 0.19 $cm^3\ g^{-1}$). The mesopores in *s*-CHA exhibited a narrow distribution of diameters centered at a size of 3.5 nm, in the pore size analysis by N_2 adsorption isotherms (Fig. 3d).

Similar to the results for CHA zeolites, the required time for complete crystallization was decreased from 8 to 2.5 days when the synthesis of FAU-X zeolites with 3 mol% OS-18 was seeded by 5 mol% bulk FAU-X zeolites. The most conspicuous difference between *s*-FAU-X and *us*-FAU-X in this synthesis case was the phase purity of the product. The major phase in *us*-FAU-X was not the FAU-X zeolites but GIS, judging from the XRD patterns presented in Fig. 4a. In contrast, the seeded synthesis yielded almost phase-pure FAU-X zeolites. The resulting *s*-FAU-X zeolites exhibited random piling of nanoplate-like crystal morphologies (Fig. 4b and c, and S7†). Fig. 4d shows the N_2 adsorption–desorption isotherms of the calcined *s*-FAU-X with its corresponding pore size distributions. A sharp increase of adsorption appeared in the relative pressure range of $0.6 < P/P_0 < 0.8$, indicating capillary condensation in mesopores. The BJH analysis derived from the adsorption branch showed a distribution of mesopores with a narrow peak centered at 6.0 nm. The *s*-FAU-X exhibited a BET surface area of 693 $m^2\ g^{-1}$ and a total pore volume of 0.50 $cm^3\ g^{-1}$.

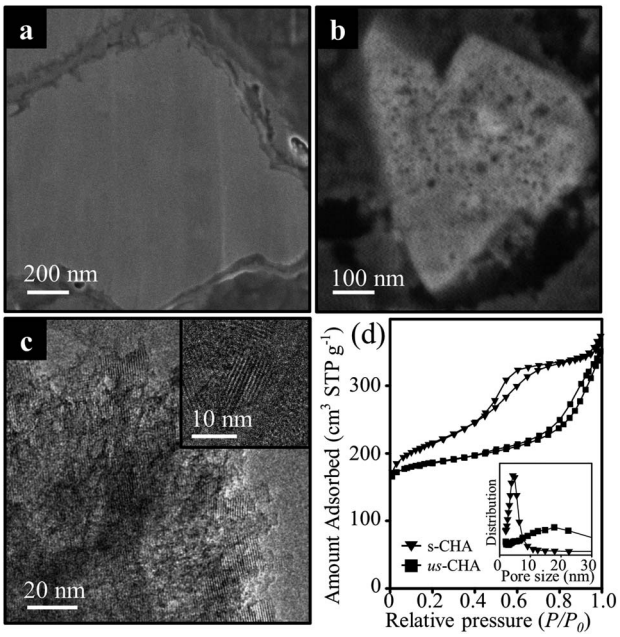

Fig. 3 SEM image of the cross-section of polished (a) *us*-CHA and (b) *s*-CHA. (c) TEM image of *s*-CHA. (d) N_2 adsorption–desorption isotherms and pore size distributions of *s*-CHA and *us*-CHA.

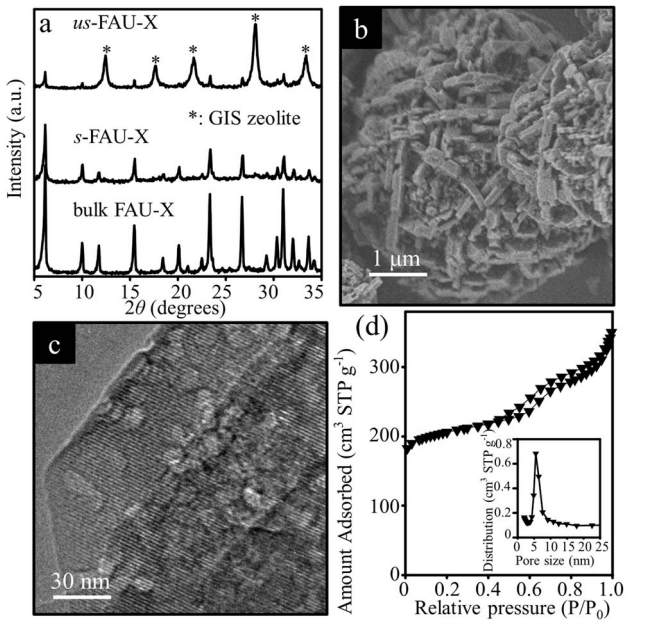

Fig. 4 (a) XRD pattern, (b) SEM image, (c) TEM image, (d) N_2 adsorption-desorption isotherms, and (inset of d) pore size distribution of *s*-FAU-X. The XRD patterns of bulk FAU-X and *us*-FAU-X zeolites are also shown in (a) for comparison. Note that some of the XRD peaks of *us*-FAU-X marked with asterisks were corresponding to those of GIS zeolites.

3.3 Friedel–Crafts alkylation over MOR zeolites

Fig. 5 shows the conversion of benzyl alcohol (BA) *versus* reaction time when benzene was alkylated to diphenylmethane (DPM) with BA, using the H^+-ion exchanged form of *s*-MOR or *c*-MOR as a catalyst. Both the *s*-MOR and *c*-MOR zeolites had the same Si/Al ratio of 7. These zeolites were fully ion-exchanged with NH_4^+, and subsequently converted to the H^+ form by calcination at 550 °C prior to their use as a catalyst. The BA/benzene mole ratio was set to 25 in the starting reaction mixture, so BA became a limiting reagent. As the result in Fig. 5 shows, the conversion of BA over *s*-MOR increased gradually with reaction time, reaching 90% in 80 h. In contrast, the *c*-MOR exhibited a conversion less than 5% at the same reaction time.

The H^+-ion exchanged form of MOR zeolite contains strong Brønsted acid sites. In principle, the acid sites can be a good catalyst for the Friedel–Crafts alkylation reaction. In fact, however, conventional MOR zeolites are not efficient catalysts. The structure of MOR zeolites is composed of one-dimensional, straight channels. Catalytic sites in such channels are susceptible to deactivation due to pore blockage by the deposition of coke polymers. Bokhoven *et al.* reported that the deactivation of the MOR catalyst in the benzylation of benzene could be effectively slowed down by the generation of mesopores through desilication.[33] The mesopore effect was attributed to facile diffusion. However, the diffusion effect does not explain the high catalytic performance of the *s*-MOR zeolites shown in Fig. 5. This zeolite sample exhibited a nanorod-like morphology, in which the one-dimensional channels ran along the longest particle dimension. The cross-sectional diameter (0.65×0.7 nm) of the zeolite channel is somewhat smaller than or close to the molecular size of the necessary transition state for benzylation to diphenylmethane. With the long nanorod morphology shown in Fig. 1, it is reasonable that the alkylation reaction would occur very slowly inside the MOR channels. We therefore attribute the high catalytic performance of *s*-MOR to reactions occurring at the mesopore walls. Svelle *et al.* reported that methylated DPM might form in the channel of MFI zeolites as a reaction intermediate during the reaction of toluene disproportionation.[34] By considering the cross-sectional diameter of the MFI zeolite channel (~0.56 nm), it seemed to be difficult for the methylated DPM to form inside the MFI zeolite framework. The MFI zeolite, however, has an intersecting two-dimensional pore structure, and the diameter of the channel intersection is 0.9 nm,[35] which is larger than that of the MOR zeolite channel (~0.7 nm). We therefore believed that the methylated DPM could be formed at the channel intersection of MFI zeolites. In addition, the reactions occurring at the mesopore walls of *s*-MOR would not be hindered by the transition-state molecular size.

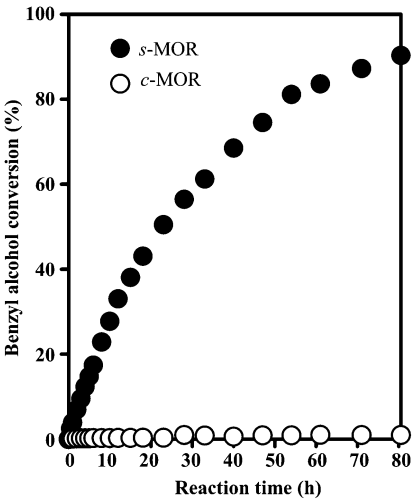

Fig. 5 Benzyl alcohol conversion over *s*-MOR and *c*-MOR zeolites, plotted as a function of reaction time (*reaction conditions*: 7.2 mmol of benzyl alcohol, 190 mmol of benzene, and 50 mg of the zeolite catalyst, reaction temperature: 353 K).

Acknowledgements

This work was supported by the Institute for Basic Science (IBS) [CA1401].

Notes and references

1 K. Na, M. Choi and R. Ryoo, *Microporous Mesoporous Mater.*, 2013, **166**, 3–19.
2 J. Pérez-Ramírez, C. H. Christensen, K. Egeblad, C. H. Chrestensen and J. C. Groen, *Chem. Soc. Rev.*, 2008, **37**, 2530–2542.
3 C. Jo, J. Jung, H. S. Shin, J. Kim and R. Ryoo, *Angew. Chem., Int. Ed.*, 2013, **52**, 10014–10017.
4 J. C. Groen, W. Zhu, S. Brouwer, S. J. Huynink, F. Kepteijin, J. A. Moulijn and J. Pérez-Ramírez, *J. Am. Chem. Soc.*, 2007, **129**, 355–360.
5 C. H. Chirstensen, K. Johannsen, E. Törnqvist, I. Schmidt, H. Topsøe and H. Christensen, *Catal. Today*, 2007, **128**, 117–122.
6 D. Mehlhorn, R. Valiullin, J. Kärger, K. Cho and R. Ryoo, *ChemPhysChem*, 2012, **13**, 1495–1499.
7 J. Kim, M. Choi and R. Ryoo, *J. Catal.*, 2010, **269**, 219–228.
8 Y. Seo, K. Cho, Y. Jung and R. Ryoo, *ACS Catal.*, 2013, **3**, 713–720.
9 M. S. Holm, E. Taarning, K. Egeblad and C. H. Christensen, *Catal. Today*, 2011, **168**, 3–16.
10 W. Kim, J.-C. Kim, J. Kim, Y. Seo and R. Ryoo, *ACS Catal.*, 2013, **3**, 192–195.
11 V. Ayala, A. Corma, M. Iglesias, J. A. Rincón and F. Sábchez, *J. Catal.*, 2004, **224**, 170–177.
12 W. Song, J. F. Woodworth, V. H. Grassian and S. C. Larsen, *Langmuir*, 2005, **21**, 7009–7014.
13 D.-H. Lee, M. Choi, B.-W. Yu and R. Ryoo, *Chem. Commun.*, 2009, 74–76.
14 J.-C. Kim, S. Lee, K. Cho and R. Ryoo, under revision.
15 C. Jo, K. Cho, J. Kim and R. Ryoo, *Chem. Commun.*, 2014, **50**, 4175–4177.
16 M. Choi, H. S. Cho, R. Srivastava, C. Venkatesan, D.-H. Choi and R. Ryoo, *Nat. Mater.*, 2006, **5**, 718–723.
17 K. Egeblad, H. Christina Christensen, M. Kustova and C. H. Christensen, *Chem. Mater.*, 2008, **20**, 946–960.

18 J. C. Groen, J. A. Moulijn and J. Perez-Ramirez, *J. Mater. Chem.*, 2006, **16**, 2121–2131.
19 C. J. H. Jacobsen, C. Madsen, J. Houzvicka, I. Schmidt and A. Carlsson, *J. Am. Chem. Soc.*, 2000, **122**, 7116–7117.
20 Y. S. Tao, H. Kanoh and K. Kaneko, *J. Am. Chem. Soc.*, 2003, **125**, 6044–6045.
21 M. Choi, K. Na, J. Kim, Y. Sakamoto, O. Terasaki and R. Ryoo, *Nature*, 2009, **461**, 246–250.
22 L. Wu, V. Degirmenci, P. C. M. M. Magusin, B. M. Szyja and E. J. M. Hensen, *Chem. Commun.*, 2012, **48**, 9492–9494.
23 A. Inayat, I. Knoke, E. Spiecker and W. Schwieger, *Angew. Chem., Int. Ed.*, 2012, **51**, 1962–1965.
24 M. Choi, R. Srivastava and R. Ryoo, *Chem. Commun.*, 2006, 4380–4382.
25 Y. Kamimura, W. Chaikittislip, K. Itabashi, A. Shimojima and T. Okubo, *Chem.–Asian J.*, 2010, **5**, 2182–2191.
26 K. Itabashi, Y. Kamimura, K. Lyoki, A. Shimojima and T. Okubo, *J. Am. Chem. Soc.*, 2012, **134**, 11542–11549.
27 S. Gonthier and R. W. Thompson, *Stud. Surf. Sci. Catal.*, 1994, **85**, 43–73.
28 G. J. Kim and W. S. Ahn, *Zeolites*, 1991, **11**, 745–750.
29 S. I. Zones and R. A. Nordstrand, *Zeolites*, 1988, **8**, 166–174.
30 H. Lechert and H. Kacirek, *Zeolites*, 1991, **11**, 720–728.
31 R. Ryoo, S. H. Joo and S. Jun, *J. Phys. Chem. B*, 1999, **103**, 7743–7746.
32 K. Cho, H. S. Cho, L.-C. de Menorval and R. Ryoo, *Chem. Mater.*, 2009, **21**, 5664–5673.
33 X. Li, R. Prins and J. A. V. Boknoven, *J. Catal.*, 2009, **262**, 257–265.
34 S. Svelle, U. Olsbye, K.-P. Lillerud, S. Kolboe and M. Bjørgen, *J. Am. Chem. Soc.*, 2006, **128**, 5618–5619.
35 B. L. Trout, A. K. Chakraborty and A. T. Bell, *Chem. Eng. Sci.*, 1997, **52**, 2265–2276.